



# Facile synthesis of porous $\text{LiMn}_2\text{O}_4$ spheres as cathode materials for high-power lithium ion batteries

YaZhou Wang<sup>a</sup>, Xuan Shao<sup>a</sup>, HaiYan Xu<sup>b</sup>, Ming Xie<sup>a</sup>, SiXu Deng<sup>a</sup>, Hao Wang<sup>a,c,\*</sup>, JingBing Liu<sup>a</sup>, Hui Yan<sup>a,c</sup>

<sup>a</sup> The College of Materials Science and Engineering, Beijing University of Technology, Beijing 100124, PR China

<sup>b</sup> Department of Materials Sciences and Engineering, Anhui University of Architecture, Hefei 230009, PR China

<sup>c</sup> Chengdu Green Energy and Green Manufacturing Technology R&D Centre, Southwest Airport Economic Development Zone, Shuangliu, Chengdu 610207, PR China

## H I G H L I G H T S

- Porous  $\text{LiMn}_2\text{O}_4$  spheres have been synthesized by a facile topochemical route.
- Molten  $\text{LiOH}$  reacted with porous  $\text{Mn}_2\text{O}_3$  spheres, which was used as a template.
- The porous sphere  $\text{LiMn}_2\text{O}_4$  revealed stable high-rate capability.

## A R T I C L E I N F O

### Article history:

Received 1 August 2012

Received in revised form

24 October 2012

Accepted 25 October 2012

Available online 2 November 2012

### Keywords:

Lithium manganese oxide

Porous spheres structure

Topochemical synthesis

Lithium ion battery

## A B S T R A C T

A facile topochemical route has been developed to synthesize porous  $\text{LiMn}_2\text{O}_4$  spheres by using molten  $\text{LiOH}$  and porous  $\text{Mn}_2\text{O}_3$  spheres as a template. The presence of pores with the average size of about 45 nm throughout the whole  $\text{LiMn}_2\text{O}_4$  microspheres was confirmed by transmission electron microscope (TEM) and  $\text{N}_2$  adsorption–desorption measurements. When applied as cathode materials for rechargeable lithium-ion batteries, the porous sphere  $\text{LiMn}_2\text{O}_4$  revealed stable high-rate capability. The discharge capacity is 83  $\text{mAh g}^{-1}$  at 20 °C rate, and it shows a good capacity retention after cycling at constantly changing discharge rate. Taking the excellent electrochemical performance and facile synthesis into consideration, the presented porous  $\text{LiMn}_2\text{O}_4$  spheres could be a competitive candidate cathode material for high-performance lithium-ion batteries.

© 2012 Elsevier B.V. All rights reserved.

## 1. Introduction

Rechargeable lithium ion batteries are regarded as promising energy storage devices for portable electronic devices as well as electric vehicles (EV) and hybrid electric vehicles (HEV), due to their high energy density, high power density, low cost, superior safety, and stable cycling lifespan [1,2]. Among various lithium-ion batteries being developed, the spinel lithium manganese oxide ( $\text{LiMn}_2\text{O}_4$ ) seems to be one of the most promising cathode materials because of its intrinsic advantages such as the abundant and cheap resources, environmental benignity, better safety, high voltage and good rate of capability [3,4]. However, along with these exceptional advantages, capacity decay and poor cycling stability of spinel

$\text{LiMn}_2\text{O}_4$  cathode materials hamper its application in commercial lithium-ion batteries [5,6]. To solve this problem, various strategies have been attempted by researchers. One has doped the heterogeneous substitution of manganese ions with a series of foreign ions, such as Li, B, Mg, Al, Co, or Zn [7,8]. Another common method is surface coating by oxides, including  $\text{ZnO}$ ,  $\text{Al}_2\text{O}_3$ ,  $\text{Co}_3\text{O}_4$  and  $\text{BiOF}$  [9–11]. Though doping and coating can indeed ameliorate the capacity fading of  $\text{LiMn}_2\text{O}_4$  spinel, this performance improvement is obtained at the expense of compromising theoretical capacity [12–14].

Other approaches to enhance the performance of  $\text{LiMn}_2\text{O}_4$  cathode have recently focused on reducing the particle size to nanoscale [15–17]. Nanomaterials facilitate rapid ionic diffusion and electronic transport due to drastically shortened transport distance, thus enabling better power performance as compared to the bulk electrode [15,18]. However, the inferior packing of nanoparticles would lead to lower volumetric energy densities unless special compaction methods are developed [18].

\* Corresponding author. The College of Materials Science and Engineering, Beijing University of Technology, Beijing 100124, PR China. Tel.: +86 10 67392733; fax: +86 10 67392445.

E-mail address: [haowang@bjut.edu.cn](mailto:haowang@bjut.edu.cn) (H. Wang).



Recently, controlled crystallization method has been used to synthesize  $\text{LiMn}_2\text{O}_4$  spinel microspheres [19]. In general, the  $\text{LiMn}_2\text{O}_4$  powder composed of spherical particles could lead to a higher tap density due to their close package, which would enhance the volumetric energy density compared with the irregularly shaped nanoparticles [20]. However, the solid sphere has very long ion and electron transportation paths compared with nanoparticles because the electrolytes cannot easily penetrate into the internal surface area of the solid spheres. Therefore, the cathode material with a porous microsphere consisted of nanocrystallites tightly compacted to form three-dimensional electronic and ionic channels should be an ideal structure [21]. Recently, Lu et al. [22] and Xi et al. [23] synthesized porous  $\text{LiMn}_2\text{O}_4$  spheres by ultrasonic spray pyrolysis process and using  $\alpha\text{-MnO}_2$  urchin-like structure as a template, respectively. However, it still remains a challenge to synthesize porous  $\text{LiMn}_2\text{O}_4$  spheres in large scale because of the complicated technology for preparation and low production yield.

Herein, we report on porous  $\text{LiMn}_2\text{O}_4$  spheres assembled by nanocrystallites as the cathode material for rechargeable lithium batteries by a topochemical reaction route. The formation of porous  $\text{LiMn}_2\text{O}_4$  spheres was inherited from porous  $\text{Mn}_2\text{O}_3$  spheres which were obtained from the thermal decomposition of the  $\text{MnCO}_3$  precursors. Significantly, without cation doping or surface coating, the porous  $\text{LiMn}_2\text{O}_4$  spheres present higher specific capacity and more stable cycle performance than those of conventional solid-state produced samples.

## 2. Experimental

The preparation of porous  $\text{LiMn}_2\text{O}_4$  spheres follows a three steps route. First, spherical  $\text{MnCO}_3$  was produced by a simple precipitation method using analytical  $\text{MnSO}_4 \cdot \text{H}_2\text{O}$  as the manganese source,  $\text{NH}_4\text{HCO}_3$  as the precipitants.  $\text{MnSO}_4 \cdot \text{H}_2\text{O}$  and  $\text{NH}_4\text{HCO}_3$  were dissolved in the distilled water with solution concentration of  $0.04 \text{ mol L}^{-1}$  and  $0.4 \text{ mol L}^{-1}$ , separately. Ethanol was added under vigorous stirring at room temperature to the stale solution of  $\text{MnSO}_4$  and  $\text{NH}_4\text{HCO}_3$ . The final concentration of ethanol in the system was 10.0% v/v. After the complete dispersion of  $\text{MnSO}_4$  and  $\text{NH}_4\text{HCO}_3$  solution, the  $\text{NH}_4\text{HCO}_3$  solution was added to the  $\text{MnSO}_4$  solution at room temperature. Then the solution turned milky white, which indicated the initial formation of  $\text{MnCO}_3$  sphere. The mixture was maintained for 1 h at room temperature and the powders obtained were leached and washed by distilled water several times and then dried in the air at  $80^\circ\text{C}$  for 24 h. Second, the obtained  $\text{MnCO}_3$  powders were heated in air at  $600^\circ\text{C}$  for 10 h (at a heating rate of about  $35^\circ\text{C min}^{-1}$ ) to synthesize porous  $\text{Mn}_2\text{O}_3$  spheres (denoted as PS- $\text{Mn}_2\text{O}_3$ ). Third, the mixtures of PS- $\text{Mn}_2\text{O}_3$  and  $\text{LiOH}$  with molar ratio of 1:1.05 were suitably ground in the agate mortar using ethanol as the disperse agent, and dried at  $80^\circ\text{C}$ , finally sintered at  $750^\circ\text{C}$  for 10 h with a heating rate of  $10^\circ\text{C min}^{-1}$  in the air, so the porous  $\text{LiMn}_2\text{O}_4$  spheres (denoted as PS- $\text{LiMn}_2\text{O}_4$ ) were achieved. For comparison, the non-porous  $\text{LiMn}_2\text{O}_4$  (denoted as NS- $\text{LiMn}_2\text{O}_4$ ) was synthesized by calcination of the mixture of electrolytic manganese dioxide (EMD) and  $\text{LiOH}$  at  $750^\circ\text{C}$  for 10 h.

X-ray power diffraction (XRD) measurements were carried out on a Shimadzu XRD diffractometer with  $\text{Cu K}\alpha$ . The morphologies and microstructures of the samples were observed using a Hitachi S4800 field emission scanning electron microscope (FESEM) and JEM 2100 transmission electron microscope (TEM) with an accelerating voltage of 200 kV. Nitrogen adsorption–desorption isotherms for surface area and pore analysis were measured with an SSA-4200 (Builder Instruments) volumetric adsorption analyzer. Before the measurement, the samples were outgassed under vacuum at  $90^\circ\text{C}$  for 5 h. Thermogravimetric and differential thermal analysis (TG-DTA) were conducted on a NETZSCH STA

449 C thermogravimetric analyzer (Germany) in the air at a scan rate of  $10^\circ\text{C min}^{-1}$  from room temperature to  $700^\circ\text{C}$ . The tap density was measured as follows: A certain quantity of a powder was added into a dry measuring cylinder. The cylinder was tapped until the volume of the powders did not change. The ratio of the mass to volume of the powders gives the tap density.

The positive electrode consisted of 80 wt.% as-prepared compounds, 10 wt.% acetylene black and 10 wt.% polyvinylidene fluoride (PVDF) as a binder. These materials were dispersed in 1-Methyl-2-pyrrolidinone (NMP), and the resultant slurry was coated onto an aluminum foil which was used as the counter electrode during the electrochemical measurements. The electrolyte was 1 M  $\text{LiPF}_6$  dissolved in a mixed solution of ethylene carbonate (EC)–dimethyl carbonate (DMC)–ethylene methyl carbonate (EMC) (1:1:1, by volume). All the simulative CR2032 coin-type cells were assembled with lithium metal as the negative electrode in an argon-filled box. The cyclic voltammogram (CV) measurements were carried out at room temperature on Model 1287 Potentiostat/Galvanostat Electrochemical Interface (Solartron Analytical, a division of AMETEK, Inc.). The electrochemical tests were carried out by a fully automatic program test instrument (BT2000, USA), with the constant current and the voltage range from 3.30 to 4.35 V (vs.  $\text{Li/Li}^+$ ).

## 3. Results and discussions

### 3.1. Synthesis and powder characterization of porous $\text{Mn}_2\text{O}_3$ spheres

Fig. 1 illustrates the XRD patterns of the as-prepared  $\text{MnCO}_3$  powder by precipitation method and manganese oxides obtained by thermal treatment of  $\text{MnCO}_3$  powders at different temperature for different intervals. All of the peaks in Fig. 1a can be readily indexed to the pure rhombohedral phase of  $\text{MnCO}_3$ . No other impurities can be detected in this XRD pattern. Upon heating  $\text{MnCO}_3$  at  $450^\circ\text{C}$  for 1 h (Fig. 1b), mixed phase of various manganese oxides including  $\alpha$ - and  $\beta$ - $\text{MnO}_2$  and  $\text{Mn}_2\text{O}_3$  can be observed. The broadening of XRD peaks suggests the small crystallite sizes of the obtained manganese oxides. After thermal treatment at  $600^\circ\text{C}$  for 1 h (Fig. 1c), the as-prepared  $\text{MnCO}_3$  are completely transformed into pure cubic phase of  $\text{Mn}_2\text{O}_3$  (JCPDS card No. 41-1442). The XRD peaks of the products at longer thermal treatment time (Fig. 1d and e) become sharper. The values of FWHM (full wave at half

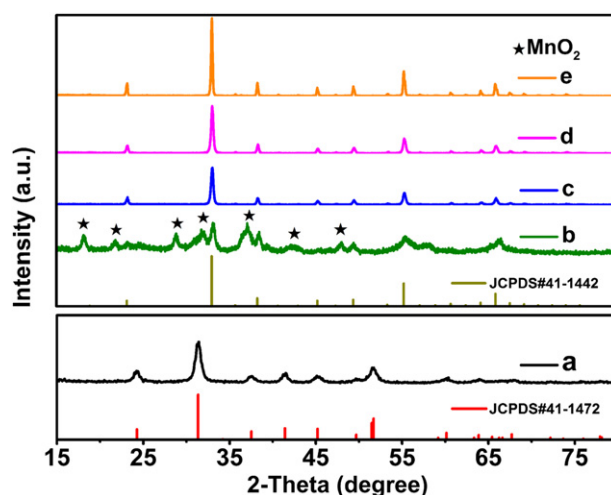


Fig. 1. XRD patterns of (a) as-prepared  $\text{MnCO}_3$  sample, the samples by heating  $\text{MnCO}_3$  at (b)  $450^\circ\text{C}$  for 1 h, and at  $600^\circ\text{C}$  for (c) 1 h, (d) 5 h, (e) 10 h.



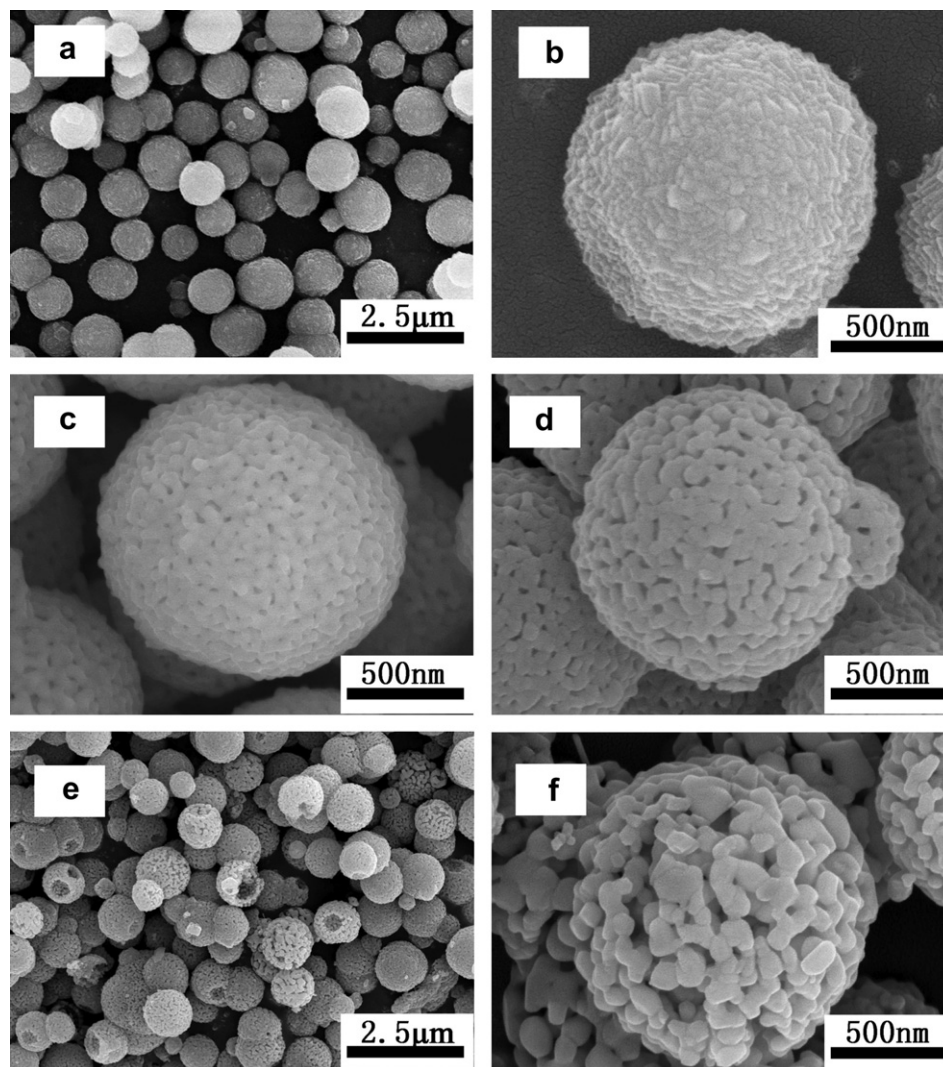


Fig. 2. SEM images of (a, b) as-prepared  $\text{MnCO}_3$  sample,  $\text{Mn}_2\text{O}_3$  powders by heating  $\text{MnCO}_3$  at  $600\text{ }^\circ\text{C}$  for (c) 1 h, (d) 5 h, (e, f) 10 h.

maximum) of the strongest characteristic peak (2-theta at  $32.87^\circ$ ) at 1 h, 5 h and 10 h are 0.339, 0.308 and 0.233, respectively. It indicates the gradual increase of crystallinity at longer thermal treatment time according to the Scherrer equation [24].

The morphologies of the samples are characterized by SEM measurements. Fig. 2a shows that the as-prepared  $\text{MnCO}_3$  powder

takes on a uniform spherical morphology with a particle size of about  $1\text{ }\mu\text{m}$ . From the high magnified image of Fig. 2b, we can see the surfaces of the  $\text{MnCO}_3$  spheres are constructed by closely packed primary nanocrystallites. The formation and evolution of

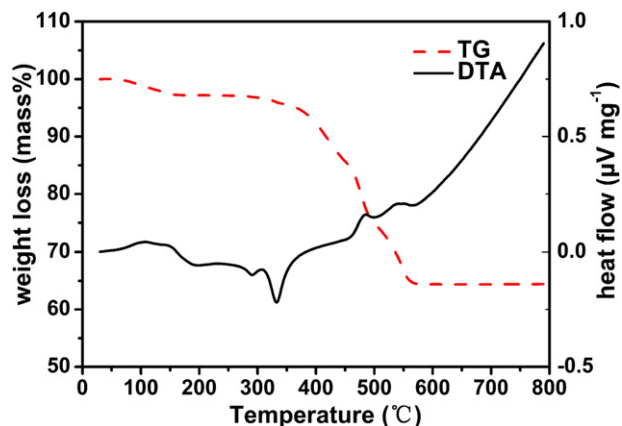


Fig. 3. DTA/TG curve of the  $\text{MnCO}_3$  thermal decomposition.

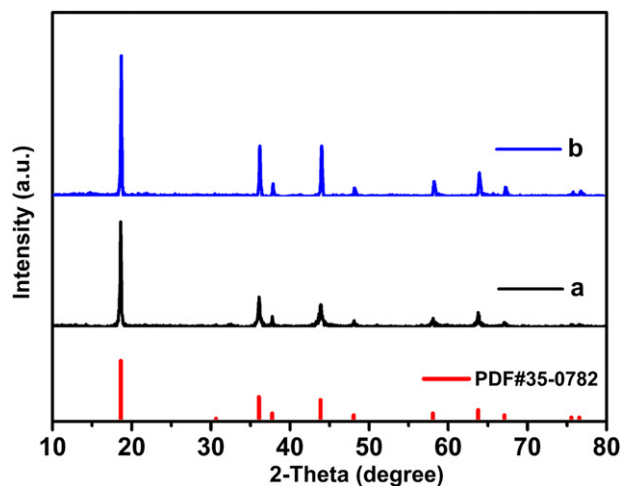


Fig. 4. XRD patterns of (a) NS- $\text{LiMn}_2\text{O}_4$ , (b) PS- $\text{LiMn}_2\text{O}_4$ .



the porous  $\text{Mn}_2\text{O}_3$  spheres by thermal treatment of  $\text{MnCO}_3$  at  $600^\circ\text{C}$  for different intervals can be visualized from Fig. 2c–f. The shapes of spherical  $\text{MnCO}_3$  are sustained after decomposition of  $\text{MnCO}_3$  into  $\text{Mn}_2\text{O}_3$ , although the oxidation state of manganese increased from +2 to +3 due to the presence of oxygen during annealing. When the annealing time is 1 h, the morphology of the obtained  $\text{Mn}_2\text{O}_3$  powder is still solid sphere with a rough surface (Fig. 2c). As increasing the annealing time to 5 h, it is clearly observed that irregularly shaped pores randomly located on the surface of the  $\text{Mn}_2\text{O}_3$  spheres (Fig. 2d). However, after annealing for 10 h, a highly porous network consisting of small  $\text{Mn}_2\text{O}_3$  units of

50–100 nm in diameter are obtained (Fig. 2e and f). It suggests that some manganese oxide primary particles crystallize out as nuclei and grow up into larger  $\text{Mn}_2\text{O}_3$  crystallites by adsorbing surrounding primary particles via Oswald ripening [25]. Noticing that the surface of the sphere in Fig. 2f is slightly loose, but the sphere is still held together as a whole. It indicates that the microstructure of these samples is quite thermally stable without structural collapse, although a few  $\text{Mn}_2\text{O}_3$  spheres break off, as shown in Fig. 2e.

TG/DTA analysis is applied to verify the decomposition process of spherical  $\text{MnCO}_3$  in Fig. 3. The first weight loss of 3% from room

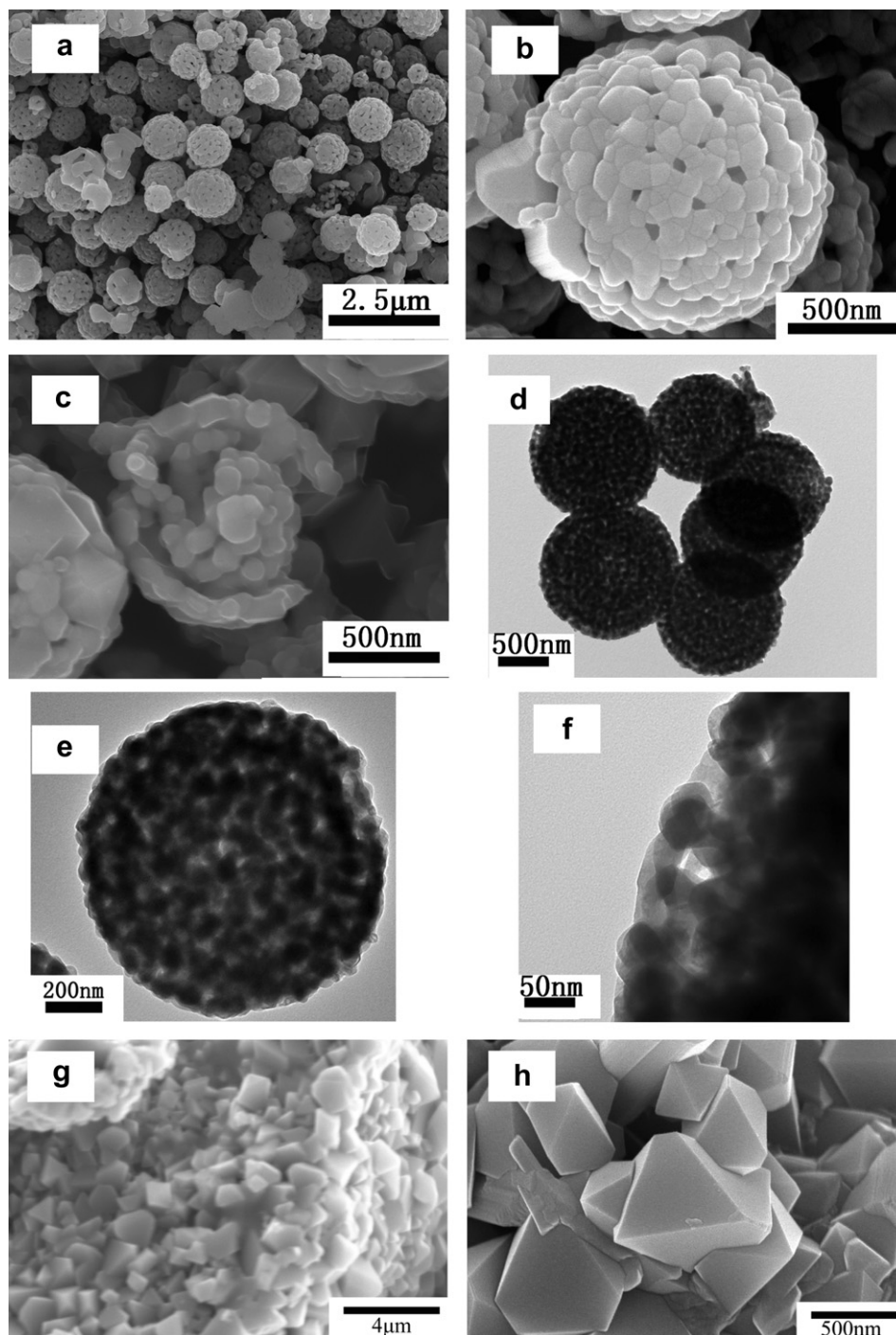
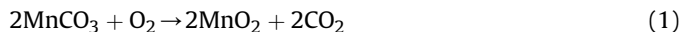


Fig. 5. SEM (a–c) and TEM (d–f) images of PS- $\text{LiMn}_2\text{O}_4$ , and SEM images (g and h) of NS- $\text{LiMn}_2\text{O}_4$ .



temperature to 150 °C in the TG curve can be attributed to the removal of hydrate water. The second significant weight loss of 32% in the temperature range of 350–560 °C, accompanying two endothermic peaks in the DTA curve, is most likely due to the thermal decomposition of  $\text{MnCO}_3$  into various manganese oxides. The chemical reactions involve in this process include:



During the decomposition process, a number of phenomena occur: the phase change in the solid state, the release of  $\text{CO}_2$  in Eq. (1), reversible oxidation and formation of various manganese oxides [26]. Finally, pure phase of  $\text{Mn}_2\text{O}_3$  is formed at above 600 °C. It is noted that the experimental weight loss for complete decomposition of  $\text{MnCO}_3$  to  $\text{Mn}_2\text{O}_3$  is 32%, which fits well theoretical value of 31.3%.

### 3.2. Synthesis and powder characterization of porous $\text{LiMn}_2\text{O}_4$ spheres

Porous  $\text{LiMn}_2\text{O}_4$  spheres (PS- $\text{LiMn}_2\text{O}_4$ ) are prepared by reaction of PS- $\text{Mn}_2\text{O}_3$  with LiOH at 750 °C for 10 h. Fig. 4 shows the XRD patterns of both PS- $\text{LiMn}_2\text{O}_4$  and NS- $\text{LiMn}_2\text{O}_4$ . The entire diffraction characteristic peaks can be clearly identified with standard orthorhombic  $\text{LiMn}_2\text{O}_4$  (JCPDS No. 35-0782). The sharp and strong XRD peaks also demonstrate the good crystallinity and high purity of the products. It indicates the successful preparation of pure phase  $\text{LiMn}_2\text{O}_4$  powders with a porous  $\text{Mn}_2\text{O}_3$  spheres precursor as conventional solid-state reaction method.

Fig. 5 gives the SEM and TEM images of PS- $\text{LiMn}_2\text{O}_4$  sample, and the SEM images of NS- $\text{LiMn}_2\text{O}_4$  (Fig. 5 g and h) as comparisons. Apparently, the porous spherical structure is well preserved in synthetic process of PS- $\text{LiMn}_2\text{O}_4$ , meaning that this unique microstructure is not collapsed and agglomerated after reaction at 750 °C for 10 h by mixing  $\text{Mn}_2\text{O}_3$  and LiOH. It is clear that these  $\text{LiMn}_2\text{O}_4$  spheres are composed of aggregated nanocrystallites with irregularly shaped pores exist among them. The size of the nanoparticles is close to 100 nm, which is slightly larger than that of incipient  $\text{Mn}_2\text{O}_3$  nanocrystallites. Meanwhile, the size of the pores obviously becomes smaller due to the growth of the primary nanocrystallites. The cross profile image of a broken sphere in Fig. 5c further reveals that there are abundant pores distributed throughout the interior

of the  $\text{LiMn}_2\text{O}_4$  sphere, constructing three-dimensional interconnected channels. TEM images (Fig. 5 d–f) also show that these pores not only exist among the surface nanocrystallites but also within the  $\text{LiMn}_2\text{O}_4$  spheres. As shown in Fig. 5 g and h, the NS- $\text{LiMn}_2\text{O}_4$  powders are packed with irregular agglomerates with the particle size of about 1  $\mu\text{m}$ .

The formation of the porous  $\text{LiMn}_2\text{O}_4$  spheres from porous  $\text{Mn}_2\text{O}_3$  spheres can be explained by the “template formation” mechanism [27]. The melting point of LiOH is 471.2 °C. Under the reaction temperature (750 °C), molten LiOH diffuses onto the surface and into the inner of the thermodynamically stable  $\text{Mn}_2\text{O}_3$  porous spheres, and then reacts with small  $\text{Mn}_2\text{O}_3$  nanocrystallites by a topochemical reaction. Therefore, the as-synthesized  $\text{LiMn}_2\text{O}_4$  products, to a large extent, inherit the morphology of porous  $\text{Mn}_2\text{O}_3$  spheres. A schematic representation of the formation of porous  $\text{LiMn}_2\text{O}_4$  spheres from porous  $\text{Mn}_2\text{O}_3$  spheres is shown in Fig. 6. From the SEM and TEM results, it can be concluded that the porous  $\text{LiMn}_2\text{O}_4$  spheres cross-linked by nanocrystallites can be synthesized by the precursor solid-state reaction with porous  $\text{Mn}_2\text{O}_3$  spheres.

To determine the pore-size distribution and Brunauer–Emmett–Teller (BET) surface area, we measure the adsorption and desorption isotherms of the PS- $\text{LiMn}_2\text{O}_4$  and NS- $\text{LiMn}_2\text{O}_4$  samples. Fig. 7 shows their  $\text{N}_2$  adsorption–desorption isotherm and the pore size distribution curve (inset). For NS- $\text{LiMn}_2\text{O}_4$ , the BET surface area is about 3.92  $\text{m}^2 \text{g}^{-1}$  and the BJH (Barret–Joyner–Halenda) average pore diameter is 11 nm. While for porous PS- $\text{LiMn}_2\text{O}_4$ , the BET surface area increases to about 26.22  $\text{m}^2 \text{g}^{-1}$  and the BJH average pore diameter increases to about 45.8 nm. In addition, NS- $\text{LiMn}_2\text{O}_4$  and PS- $\text{LiMn}_2\text{O}_4$  show a similar  $\text{N}_2$  adsorption and desorption isotherm corresponding to type V isotherm, but the  $\text{N}_2$  adsorption quantity for porous  $\text{LiMn}_2\text{O}_4$  is much higher than that of NS- $\text{LiMn}_2\text{O}_4$ , indicating the abundance of mesopores in porous PS- $\text{LiMn}_2\text{O}_4$ , which is in good agreement with those observed in SEM and TEM images. The data implies that the porous  $\text{LiMn}_2\text{O}_4$  spheres possess a high contact area with the electrolyte and hence a high lithium-ion flux across the interface [18].

### 3.3. Electrochemical performance of spinel $\text{LiMn}_2\text{O}_4$

The electrochemical performance of porous  $\text{LiMn}_2\text{O}_4$  spheres is discussed as a cathode material for a lithium-ion rechargeable battery. Especially, we focus on the durability on the constant

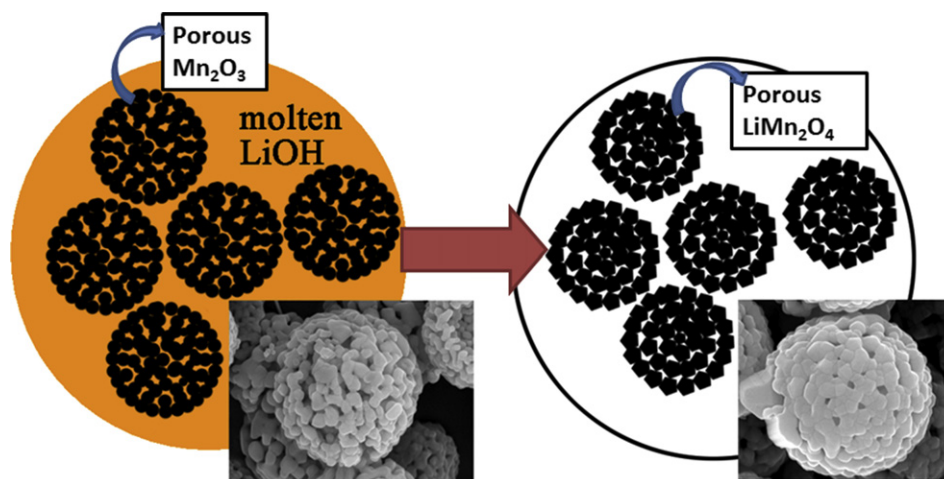


Fig. 6. A schematic representation of the formation of porous  $\text{LiMn}_2\text{O}_4$  spheres from porous  $\text{Mn}_2\text{O}_3$  spheres.



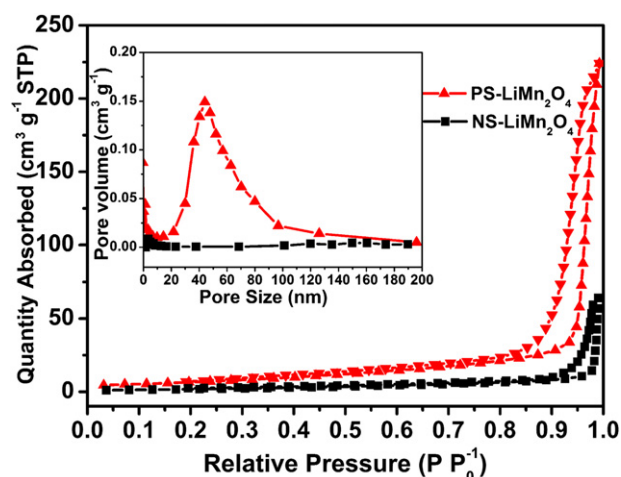


Fig. 7. Nitrogen adsorption/desorption isotherm and Barrett–Joyner–Halenda (BJH) pore size distribution plot (inset) of PS-LiMn<sub>2</sub>O<sub>4</sub> and NS-LiMn<sub>2</sub>O<sub>4</sub>.

current charge/discharge measurement by different rates over the voltage range of 3.3–4.35 V and the results are shown in Fig. 8a. The first discharge capacities of the PS-LiMn<sub>2</sub>O<sub>4</sub> are 128, 125, 118, 109, 98 and 83 mAh g<sup>-1</sup> at 0.2, 1, 2, 5, 10 and 20 C, respectively. It is notable that the capacity retention rate at 20 C maintained nearly 65% of its capacity compared with 0.2 C. It suggests that the large surface area and the short diffusion length of porous sphere structured spinel electrodes improve the kinetic properties of the lithium-ion during intercalation and easily deliver high discharge capacity even under extremely high currents. Fig. 8b reveals the cycle performance of the PS-LiMn<sub>2</sub>O<sub>4</sub> and NS-LiMn<sub>2</sub>O<sub>4</sub> at 1 C rate. After 100 cycles at 1 C rate, the discharge capacity of the PS-LiMn<sub>2</sub>O<sub>4</sub> is still maintained 94% of its capacity compared with first cycle, which is much higher than 78% of the NS-LiMn<sub>2</sub>O<sub>4</sub> capacity maintained. Fig. 8c compares the rate capability of the PS-LiMn<sub>2</sub>O<sub>4</sub> and NS-LiMn<sub>2</sub>O<sub>4</sub> with charge/discharge rates of 1 C–20 C. PS-LiMn<sub>2</sub>O<sub>4</sub> shows obviously slower capacity decay with increasing discharge rates. It presents a slowly declining trend up to 20 C, reaching a discharge capacity of 80 mAh g<sup>-1</sup>. On the contrary, the capacity of NS-LiMn<sub>2</sub>O<sub>4</sub> is found to decay quickly at high discharge rate. It is only 18 mAh g<sup>-1</sup> at 10 C, and is almost undetectable at 20 C. After 200 cycles with discharge rate constantly changing, the discharge capacity of PS-LiMn<sub>2</sub>O<sub>4</sub> is still maintained 118 mAh g<sup>-1</sup> when the rate comes back to 1 C; however, NS-LiMn<sub>2</sub>O<sub>4</sub> shows a capacity of only 55 mAh g<sup>-1</sup> at the same rate. The good capacity retention for PS-LiMn<sub>2</sub>O<sub>4</sub> after cycling at constantly changing discharge rate suggests that its structure is stable. Evidently, the excellent rate capability is due to abundant porous structure and high active surface area. Such behavior coincides with consequence of SEM, TEM and BET analysis.

To gain the electrochemical characteristics of the porous LiMn<sub>2</sub>O<sub>4</sub> spheres as a cathode for a lithium-ion rechargeable battery, we perform a series of voltammetry measurements. Fig. 9a and b shows the cyclic voltammogram (CV) of the PS-LiMn<sub>2</sub>O<sub>4</sub> and NS-LiMn<sub>2</sub>O<sub>4</sub> recorded at 0.1 mV s<sup>-1</sup>–0.5 mV s<sup>-1</sup> scan rates, respectively. With the increase of the scan rate to 0.5 mV s<sup>-1</sup>, the separation of the NS-LiMn<sub>2</sub>O<sub>4</sub> between two redox pair becomes indistinguishable (Fig. 9b), which is due to the polarization of the electrode process increases gradually. In contrast, the separation of the PS-LiMn<sub>2</sub>O<sub>4</sub> is still clearly visible (Fig. 9a). The CV curve of the PS-LiMn<sub>2</sub>O<sub>4</sub> and NS-LiMn<sub>2</sub>O<sub>4</sub> at the 0.1 mV s<sup>-1</sup> scan rate as shown in Fig. 9c, two couples of separate redox peaks (the anodic peak  $E_{a1}$  and  $E_{a2}$ , the cathodic peak  $E_{c1}$  and  $E_{c2}$ ) are observed from the CV

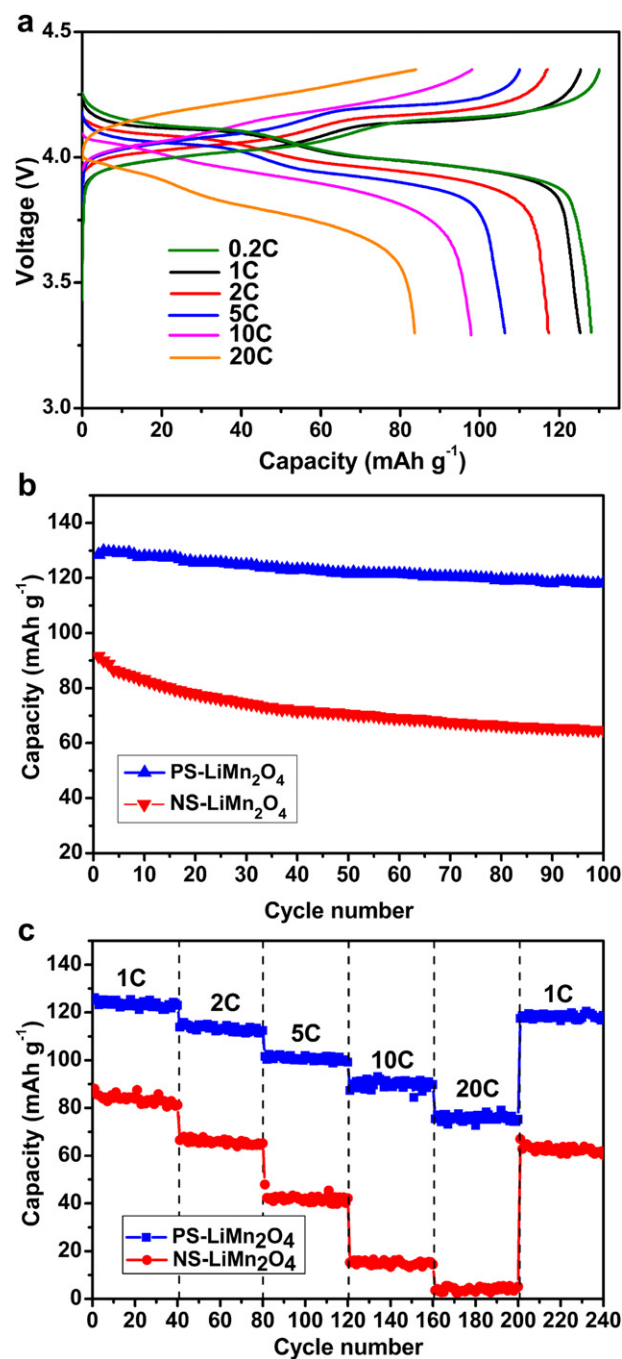


Fig. 8. (a) Charge and discharge curves of the PS-LiMn<sub>2</sub>O<sub>4</sub> at different rates, (b) cycle performance of the PS-LiMn<sub>2</sub>O<sub>4</sub> and NS-LiMn<sub>2</sub>O<sub>4</sub> at 1 C rate, and (c) variation of discharge capacity vs. cycle number of PS-LiMn<sub>2</sub>O<sub>4</sub> and NS-LiMn<sub>2</sub>O<sub>4</sub> electrodes at the 1, 2, 5, 10, and 1 C rates.

curves of both PS-LiMn<sub>2</sub>O<sub>4</sub> and NS-LiMn<sub>2</sub>O<sub>4</sub>, which are corresponding to the two-step intercalation/deintercalation of Li<sup>+</sup> into/from the spinel phase and the detected two-plateau charge/discharge profile [28]. It shows that the porous LiMn<sub>2</sub>O<sub>4</sub> spheres electrode reveals higher charge/discharge peak current and smaller voltage gap between the discharge and the charge curves. Fig. 9d indicate the peak currents vs. the square root of the scan rates of PS-LiMn<sub>2</sub>O<sub>4</sub> and NS-LiMn<sub>2</sub>O<sub>4</sub> shows a linear increase, which suggests that the intercalation reaction is controlled by solid-state diffusion of lithium-ion [29]. Moreover, for a reversible reaction relating lithium-ion diffusion behavior, the diffusion coefficient of



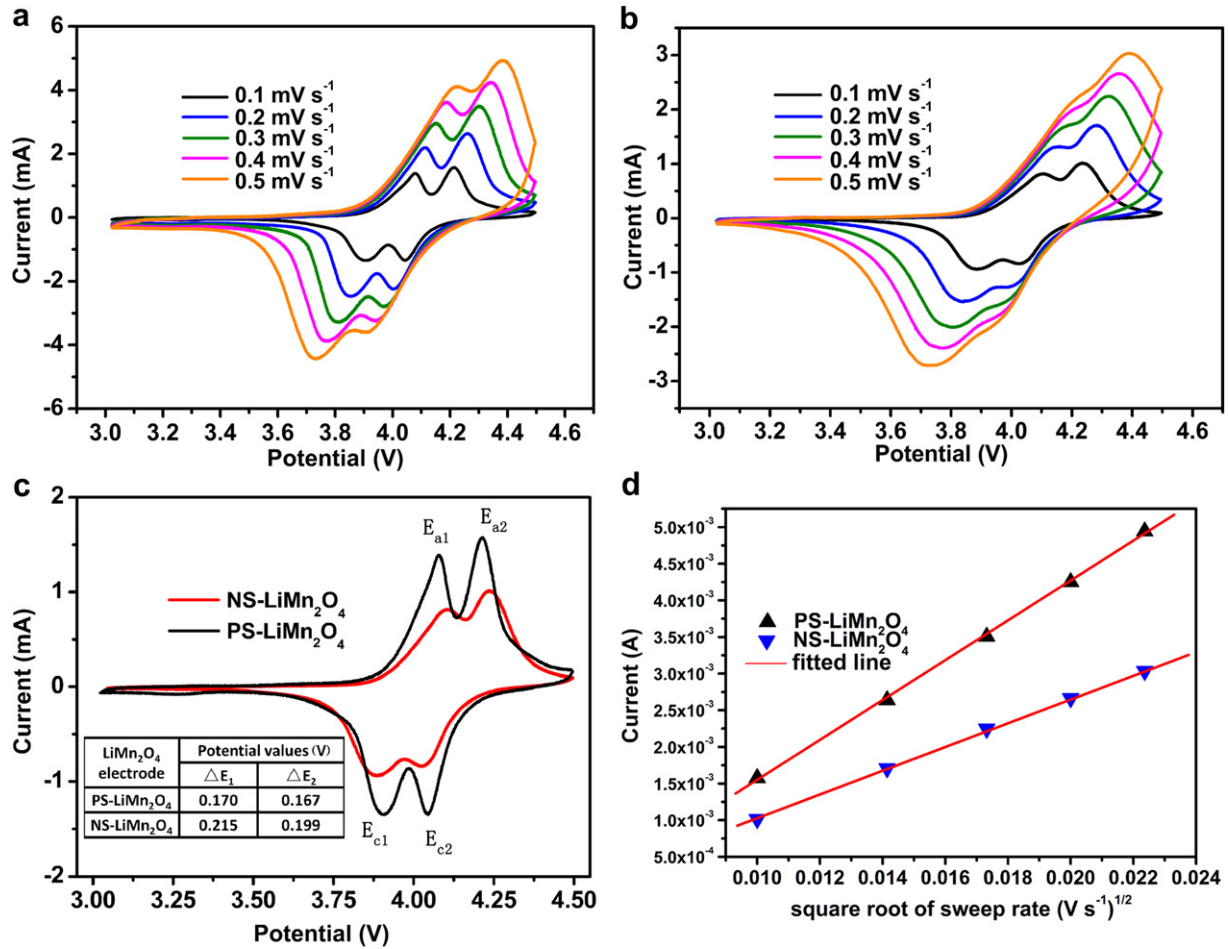


Fig. 9. Cyclic voltammogram (CV) of the electrodes made with (a) PS-LiMn<sub>2</sub>O<sub>4</sub>, and (b) NS-LiMn<sub>2</sub>O<sub>4</sub> at different scan rates. (c) Comparison of the CV recorded at the scan rate of 0.1 mV s<sup>-1</sup> of PS-LiMn<sub>2</sub>O<sub>4</sub> and NS-LiMn<sub>2</sub>O<sub>4</sub>, (d) the plotting of peak current vs. square root of the scan rate for PS-LiMn<sub>2</sub>O<sub>4</sub> and NS-LiMn<sub>2</sub>O<sub>4</sub>.

lithium-ion ( $D_{Li}$ ) can be determined on the basis of the following Randles-Sevcik equation [30]:

$$i_p = 0.4463 n^2 F^3 C_{Li} A R^{-1/2} T^{-1/2} D_{Li}^{1/2} v^{1/2} \quad (3)$$

At 25 °C:

$$i_p = (2.69 \times 10^5) n^2 C_{Li} A D_{Li}^{1/2} v^{1/2} \quad (4)$$

where  $i_p$  is the peak current value (A),  $n$  is the number of electrons per reaction species (for lithium-ion  $n = 1$ ),  $C_{Li}$  is the bulk concentration of lithium-ion in the electrode (0.0238 mol cm<sup>-3</sup> for LiMn<sub>2</sub>O<sub>4</sub> derived from the theoretical density of 4.3 g cm<sup>-3</sup>),  $A$  is the surface area of electrode (cm<sup>2</sup>),  $D_{Li}$  is the chemical diffusion coefficient (cm<sup>2</sup> s<sup>-1</sup>), and  $v$  is the scanning rate (V s<sup>-1</sup>). From the slope of linear fit of the peak current ( $i_p$ ) vs. the square root of the scan rates ( $v^{1/2}$ ) in Fig. 9d, the diffusion coefficients ( $D_{Li}$ ) of PS-LiMn<sub>2</sub>O<sub>4</sub> and NS-LiMn<sub>2</sub>O<sub>4</sub> have been calculated, which are  $4.61 \times 10^{-10}$  and  $1.66 \times 10^{-10}$  cm<sup>2</sup> s<sup>-1</sup> respectively. Hence, the larger  $D_{Li}$  is obtained for the porous LiMn<sub>2</sub>O<sub>4</sub> sphere as compared to the conventional solid-state sample. It is known that the chemical diffusion coefficient increases with the increase of the BET surface area. Thus, the higher BET surface areas of the PS-LiMn<sub>2</sub>O<sub>4</sub> and its unique porous microstructures consisting of nanoparticles compacted to form three-dimensional channels are very favorable for lithium ion diffusion [23]. Moreover, the micron-sized spheres are also expected to provide a higher tap density compared with

nanostructured electrode materials. The tap density of the PS-LiMn<sub>2</sub>O<sub>4</sub> is about 1.4 g cm<sup>-3</sup>, which is slightly larger than the value of 1.2 g cm<sup>-3</sup> of the NS-LiMn<sub>2</sub>O<sub>4</sub> sample. The lower tap density of the NS-LiMn<sub>2</sub>O<sub>4</sub> powders might be ascribed to their irregular shapes. Generally the closely packed uniform spherical particles would have higher tap density [31].

Fig. 10 shows the electrochemical impedance spectra (EIS) of the batteries with different samples as electrodes after 5th cycled. The plot includes the real component of the impedance on the horizontal axis ( $Z'$ ), and the imaginary component of the impedance on the vertical axis ( $Z''$ ). The EIS spectrums are combination of the depressed semicircle at high-to-middle frequency region and an inclined line in the low frequency region. The intercept at the  $Z'$  axis corresponds to the ohmic resistance ( $R_s$ ), the semicircle is related closely to the lithium-ion migration resistance ( $R_f$ ) through the multilayer surface films and the charge transfer resistance ( $R_{ct}$ ) in high-to-middle frequency range. Apparently, it can be seen from Fig. 10a (inset) that  $R_{ct}$  of the PS-LiMn<sub>2</sub>O<sub>4</sub> is lower than that of the NS-LiMn<sub>2</sub>O<sub>4</sub> sample. The higher charge transfer resistance ( $R_{ct}$ ) of the NS-LiMn<sub>2</sub>O<sub>4</sub> cell signifies the more capacity loss in the high charge/discharge rate, which is in good agreement with the C-rate capacity data. Furthermore, the inclined line in the low frequency region which is related to the lithium-ion diffusion in the LiMn<sub>2</sub>O<sub>4</sub> particles represents the Warburg impedance ( $\sigma_w$ ) [32]. The parameters of impedance spectra is simulated and fitted with an equivalent circuit by ZView software as shown in Fig. 10a. The Warburg coefficient  $\sigma_w$  can be calculated by following equation [33]:



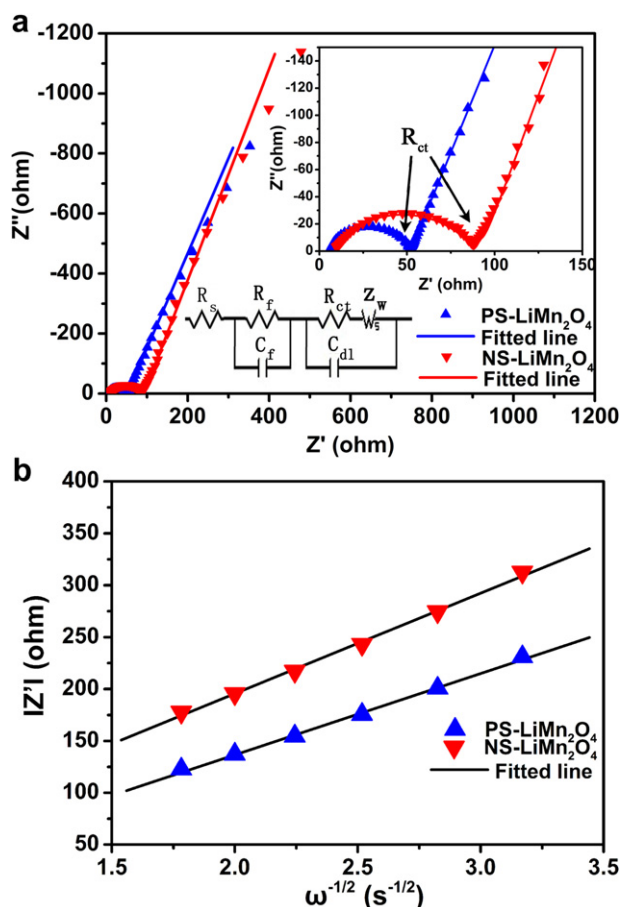


**Fig. 10.** (a) EIS spectra of the PS-LiMn<sub>2</sub>O<sub>4</sub> and NS-LiMn<sub>2</sub>O<sub>4</sub> in the frequency range between 0.1 Hz and 100 kHz. (b) The relationship between  $Z'$  and  $\omega^{-1/2}$  at low frequencies for the PS-LiMn<sub>2</sub>O<sub>4</sub> and NS-LiMn<sub>2</sub>O<sub>4</sub>.

$$|Z'| = R_s + R_{ct} + \sigma_w \omega^{-0.5} \quad (5)$$

Both  $R_s$  and  $R_{ct}$  are kinetic parameters independent of frequency. In addition, the plot of  $Z'$  vs. the reciprocal square roots of the lower angular frequencies ( $\omega^{-0.5}$ ) of PS-LiMn<sub>2</sub>O<sub>4</sub> and NS-LiMn<sub>2</sub>O<sub>4</sub> is shown in Fig. 10b. So, the slope of the fitted line obtained in Fig. 10b is the Warburg coefficient  $\sigma_w$ . Moreover, Warburg coefficients ( $\sigma_w$ ) are also calculated for in PS-LiMn<sub>2</sub>O<sub>4</sub> and NS-LiMn<sub>2</sub>O<sub>4</sub> electrodes and the value is 81.23 and 101.57  $\Omega \text{cm}^2 \text{s}^{-0.5}$ , respectively. Therefore, the relationship of diffusion coefficient of the lithium-ion ( $D_{Li}$ ) and Warburg coefficient  $\sigma_w$  is,  $D_{Li}$  decrease with the increase of  $\sigma_w$  [34]. Consequently, the sample of PS-LiMn<sub>2</sub>O<sub>4</sub> shows the higher lithium-ion diffusion coefficient compared with the NS-LiMn<sub>2</sub>O<sub>4</sub>. The aforementioned results of charge/discharge and cyclic voltammetry (CV) measurement are consistent with the analysis of the EIS spectrum.

Above all, compared with the solid LiMn<sub>2</sub>O<sub>4</sub> spheres [35], the porous structure can improve the Li-ion diffusion coefficients, which has been confirmed by pertinent literature [15,17,36]. The solid spheres have very long ion and electron transportation paths compared with nanoparticles because the electrolytes cannot easily penetrate into the internal surface area of the solid spheres. On the other hand, compared with the hollow structure LiMn<sub>2</sub>O<sub>4</sub> [37,38], the porous structure can contain more active cathode materials, which might result in higher energy densities. Furthermore, the preparation method of the PS-LiMn<sub>2</sub>O<sub>4</sub> in this study is much more facile and cheaper than those of hollow structures.

## 4. Conclusions

In summary, we have successfully developed a facile method to synthesize porous LiMn<sub>2</sub>O<sub>4</sub> spheres. This method takes advantage of molten LiOH and porous Mn<sub>2</sub>O<sub>3</sub> spheres as a template by a topochemical reaction. The presence of pores with the average size of about 45 nm throughout the whole LiMn<sub>2</sub>O<sub>4</sub> microspheres and the pore-size distribution were confirmed by TEM and N<sub>2</sub> adsorption–desorption measurements. When applied as cathode materials for rechargeable lithium-ion batteries, the porous sphere LiMn<sub>2</sub>O<sub>4</sub> revealed stable high-rate capability. The discharge capacity is 83 mAh g<sup>-1</sup> at 20 C rate, and it shows a good capacity retention after cycling at constantly changing discharge rate. The excellent high rate capability for porous LiMn<sub>2</sub>O<sub>4</sub> spheres maybe due to its porous morphology consisting of nanocrystallites tightly compacted to form three-dimensional channels which are extraordinarily suitable for lithium ion diffusion. It is believed that this synthetic method would be easily extended to large-scale production. Taking the excellent electrochemical performance and facile synthesis into consideration, the presented porous LiMn<sub>2</sub>O<sub>4</sub> spheres could be a competitive candidate cathode material for high-performance lithium-ion batteries used for electric vehicles (EV) and hybrid electric vehicles (HEV) in the near future.

## Acknowledgments

This work is supported by the Project for Academic Human Resources Development in Institutions of Higher Learning under the Jurisdiction of Beijing Municipality, PHR (IHLB).

## References

- [1] B. Scrosati, *Nature* 373 (1995) 557–558.
- [2] M. Armand, J.M. Tarascon, *Nature* 451 (2008) 652–657.
- [3] G. Amatucci, J.-M. Tarascon, *J. Electrochem. Soc.* 149 (2002) K31–K46.
- [4] D.K. Kim, P. Muralidharan, H.W. Lee, R. Ruffo, Y. Yang, C.K. Chan, H. Peng, R.A. Huggins, Y. Cui, *Nano Lett.* 8 (2008) 3948–3952.
- [5] M.M. Thackeray, *Prog. Solid State Chem.* 25 (1997) 1–71.
- [6] J. Arai, T. Yamaki, S. Yamauchi, T. Yuasa, T. Maeshima, T. Sakai, M. Koseki, T. Horiba, *J. Power Sources* 146 (2005) 788–792.
- [7] J.S. Gnanaraj, V.G. Pol, A. Gedanken, D. Aurbach, *Electrochem. Commun.* 5 (2003) 940–945.
- [8] B.H. Deng, H. Nakamura, Q. Zhang, M. Yoshio, Y.Y. Xia, *Electrochim. Acta* 49 (2004) 1823–1830.
- [9] Y.K. Sun, K.J. Hong, J. Prakash, *J. Electrochem. Soc.* 150 (2003) A970–A972.
- [10] S.-T. Myung, K. Izumi, S. Komaba, Y.-K. Sun, H. Yashiro, N. Kumagai, *Chem. Mater.* 17 (2005) 3695–3704.
- [11] K.-S. Lee, S.-T. Myung, H. Bang, K. Amine, D.-W. Kim, Y.-K. Sun, *J. Power Sources* 189 (2009) 494–498.
- [12] G. Amatucci, A. Du Pasquier, A. Blyr, T. Zheng, J.M. Tarascon, *Electrochim. Acta* 45 (1999) 255–271.
- [13] S.-W. Lee, K.-S. Kim, H.-S. Moon, H.-J. Kim, B.-W. Cho, W.-I. Cho, J.-B. Ju, J.-W. Park, *J. Power Sources* 126 (2004) 150–155.
- [14] K.-S. Lee, S.-T. Myung, K. Amine, H. Yashiro, Y.-K. Sun, *J. Mater. Chem.* 19 (2009) 1995–2005.
- [15] F. Cheng, H. Wang, Z. Zhu, Y. Wang, T. Zhang, Z. Tao, J. Chen, *Energy Environ. Sci.* 4 (2011) 3668–3675.
- [16] K.M. Shaju, P.G. Bruce, *Chem. Mater.* 20 (2008) 5557–5562.
- [17] J. Cabana, T. Valdés-Solís, M.R. Palacín, J. Oró-Solé, A. Fuertes, G. Marbán, A.B. Fuertes, *J. Power Sources* 166 (2007) 492–498.
- [18] A.S. Arico, P. Bruce, B. Scrosati, J.M. Tarascon, W. Van Schalkwijk, *Nat. Mater.* 4 (2005) 366–377.
- [19] H.L. Zhu, Z.Y. Chen, S. Ji, V. Linkov, *Solid State Ion.* 179 (2008) 1788–1793.
- [20] X. He, J. Li, Y. Cai, C. Jiang, C. Wan, *Mater. Chem. Phys.* 95 (2006) 105–108.
- [21] J. Qian, M. Zhou, Y. Cao, X. Ai, H. Yang, *J. Phys. Chem. C* 114 (2010) 3477–3482.
- [22] C.H. Lu, T.Y. Wu, H.C. Wu, M.H. Yang, Z.Z. Guo, I. Taniguchi, *Mater. Chem. Phys.* 112 (2008) 115–119.
- [23] L.J. Xi, H.-E. Wang, Z.G. Lu, S.L. Yang, R.G. Ma, J.Q. Deng, C.Y. Chung, *J. Power Sources* 198 (2012) 251–257.
- [24] H.G. Jiang, M. Ruhle, E.J. Laverna, *J. Mater. Res.* 14 (1999) 549–559.
- [25] C. Yu, L. Zhang, J. Shi, J. Zhao, J. Gao, D. Yan, *Adv. Funct. Mater.* 18 (2008) 1544–1554.
- [26] L. Biernacki, S. Pokrzywnicki, *J. Therm. Anal. Calorim.* 55 (1999) 227–232.



- [27] L. Li, J. Deng, J. Chen, X. Sun, R. Yu, G. Liu, X. Xing, *Chem. Mater.* 21 (2009) 1207–1213.
- [28] M.M. Thackeray, W.I.F. David, P.G. Bruce, J.B. Goodenough, *Mater. Res. Bull.* 18 (1983) 461–472.
- [29] S.R. Das, S.B. Majumder, R.S. Katiyar, *J. Power Sources* 139 (2005) 261–268.
- [30] R.S. Nicholson, *Anal. Chem.* 37 (1965) 1351–1355.
- [31] C. Wan, M. Cheng, D. Wu, *Powder Technol.* 210 (2011) 47–51.
- [32] K.A. Striebel, E. Sakai, E.J. Cairns, *J. Electrochem. Soc.* 149 (2002) A61–A68.
- [33] Y. Cui, X.L. Zhao, R.S. Guo, *Electrochim. Acta* 55 (2010) 922–926.
- [34] D.E. Smith, *Anal. Chem.* 38 (1966) 347–351.
- [35] I. Taniguchi, C.K. Lim, D. Song, M. Wakihara, *Solid State Ion.* 146 (2002) 239–247.
- [36] Y. Wu, Z. Wen, H. Feng, J. Li, *Small* 8 (2012) 858–862.
- [37] X. Zhao, M.V. Reddy, H. Liu, S. Ramakrishna, G.V.S. Rao, B.V.R. Chowdari, *RSC Adv.* 2 (2012) 7462–7469.
- [38] D. Wang, X. Ma, Y. Wang, L. Wang, Z. Wang, W. Zheng, X. He, J. Li, Q. Peng, Y. Li, *Nano Res.* 3 (2010) 1–7.